REYNOLDS STRESS ANISOTROPY IN SHOCK-CONTAINING JETS

Daniel Edgington-Mitchell, Paul Stegeman, Vassili Kitsios, Damon Honnery
Laboratory For Turbulence Research in Aerospace and Combustion,
Department of Mechanical and Aerospace Engineering, Monash University, Clayton 3800, AUSTRALIA
daniel.m.mitchell@gmail.com

Andrew Ooi
Department of Mechanical Engineering, The University of Melbourne, Victoria 3010, AUSTRALIA

Julio Soria
Laboratory For Turbulence Research in Aerospace and Combustion,
Department of Mechanical and Aerospace Engineering, Monash University, Clayton 3800, AUSTRALIA
Department of Aeronautical Engineering, King Abdulaziz University,
Jeddah 21589, KINGDOM OF SAUDI ARABIA

ABSTRACT

The anisotropy of the Reynolds stress tensor is assessed from numerical and experimental data for an under-expanded supersonic jet. Shock structures are shown both to directly influence anisotropy within the jet core, as well as to modulate anisotropy within the shear layer. The jet shear layer is mostly characterized by three-component turbulence, with complex variation within the jet core due to both shock and expansion structures, as well as the interior shear layer generated from the Mach disk triple point.

Introduction

Supersonic jet flows are frequently accompanied by the presence of intense sound produced via several separate mechanisms (Tam, 1995). Amongst the identified mechanisms are jet screech, broad-band shock associated noise (BBSAN), and turbulent mixing noise. The first two mechanisms are unique to shock containing supersonic flows, while turbulent mixing noise is present in all aerodynamic flows.

While there are various methodologies available to remove screech from a flow and ameliorate BBSAN, turbulent mixing noise remains a concern for both subsonic and supersonic jets. Thus understanding the mechanisms of turbulent mixing noise generation, and consequently how they can be suppressed, remains a key focus. The prediction of jet noise has typically been attempted through the use of acoustic analogies such as those introduced by Lighthill (1952). The accuracy of these analogies is dependent on how well the underlying assumptions capture the true dynamics of the flow. Classical models for the prediction of aerodynamic noise have typically been founded on an assumption of isotropic turbulence (Ribner, 1969; Lilley, 1948). Deviation from isotropy in the turbulent fluctuations has been shown theoretically to influence acoustic di-rectionality (Goldstein & Rosenbaum, 1973) and amplitude (Khavaran, 1999). It has been established for some time that the turbulence in jet flows is highly anisotropic, for jets ranging from the low subsonic (Bradshaw *et al.*, 1964) to the transonic. Much of the experimental determination of turbulent anisotropy has been conducted in shock-free jets. Prior work has shown that the presence of shocks within the jet modulates some components of the turbulence, but not others (Edgington-Mitchell *et al.*, 2014*b*). This paper thus sets out to establish the degree to which the presence of shock structures within the flow affects the degree of turbulent anisotropy. High-resolution particle image velocimetry measurements combined with high-fidelity Large Eddy Simulation (LES) results are analyzed to assess the anisotropy of the Reynolds stress tensor.

Methodology

The particle image velocimetry experiments to produce the velocity data presented herein have been discussed previously in some detail Mitchell *et al.* (2013). Particle images were acquired using a pair of PCO 4000 cameras with an array size of 4008 x 2760 pixels, mounted perpendicular to the jet with a combined field of view of $2.2D$ in the radial and $10D$ in the axial directions. The cameras were fitted with 105mm Micro Nikkor Nikon lenses set at an aperture of $f/5.6$. Illumination was supplied by a New Wave Solo PIV Nd:YAG laser at 532nm wavelength. A multigrid cross-correlation algorithm was used to analyze the image pairs (Soria, 1996); IW_0 represents initial interrogation window size, and IW_1 represents final interrogation window size. A conservative estimate of the minimum resolvable displacement in the PIV measurements of 0.1px has been used to estimate the smallest measurable velocity fluctuation as 1.5%. A minimum velocity fluctuation of 1.5% was used in the calculation of all anisotropies presented herein.

Table 1. Non-dimensional PIV Parameters	
Parameter	Non-Dimensional Value
IW_0	0.10D
IW_1	0.026D
Grid Spacing	0.013D
Depth of Field	0.17D
Light Sheet Thickness	0.1D
Field of View	10D x 2.2 D
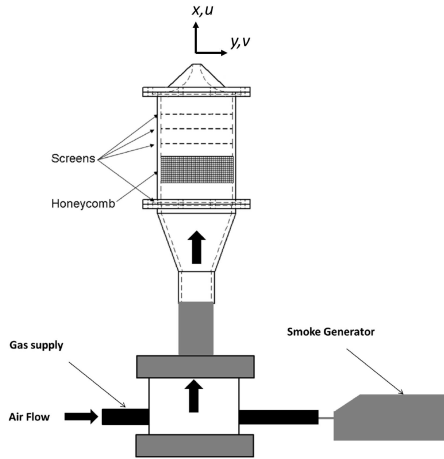
Figure 1. Schematic of the LTRAC Supersonic Jet Facility. Smoke particles for PIV seeding are mixed with the primary air supply prior to entry into the plenum. Adapted from Mitchell *et al.* (2013).

The numerical dataset used in this study is the result of a three dimensional hybrid large-eddy simulation on a non-uniform structured cylindrical grid. For spatial differentiation the hybrid solver employs a sixth order central nite difference scheme for smooth regions and a fifth order weighted essentially non-oscillatory scheme with local Lax-Friedrichs flux splitting in discontinuous regions. Temporal integration is performed using a fourth order five step Runge-Kutta scheme. The sub-grid scale terms were computed using Germanos dynamic model with the adjustments made by Lilly (1992).

The domain consists of approximately 16.4 million nodes with the spatial extent of $30D$ downstream and $15D$ the radial direction. Locally one-dimensional inviscid compressible boundary conditions defined in Poinsot (1992) are used for the adiabatic nozzle wall and outflow regions. Sponge regions are employed near the outflow boundary were the flow field is forced to a self similar incompressible jet solution that has been determined *a priori*. The jet inlet velocity profile was modeled using the hyperbolic-tangent function found in Bodony & Lele (2005) while the temperature profile was determined using the Crocco-Busemann relationship Schlichting & Gersten (2000).

An underexpanded jet is characterized principally by the nozzle pressure ratio, defined as the ratio of pressure between the plenum and the ambient condition: $NPR = P_0/P_a$. The simulations are intended to represent a canonical case, rather than directly emulating the experimental setup. The nozzle used in the experiment has a 5mm nozzle lip thickness; the numerical simulation has the jet issuing from a bluff body. The inlet to the flow is not seeded with initial turbulence, which influences the development of the shear layer near the nozzle. The Reynolds number for the simulation of the NPR = 4.2 jet is $Re = 5.0 \times 10^4$, whereas it is $Re = 8.3 \times 10^5$ for the experiment.

Results

As the experimental measurements are limited to two-component planar PIV, a consideration of the Reynolds stress anisotropy is similarly limited to considering only the axial ($\overline{u'u'}$) and transverse ($\overline{v'v'}$) stresses. Here u' is defined as per the classical decomposition of velocity into mean and fluctuating components: $u = \overline{u} + u'$. Figure 2 presents planar maps of this two-component anisotropy of the Reynolds stresses ($\frac{\overline{u'u'}}{\overline{v'v'}}$) for jets ranging in pressure ratio from NPR = 2.2 to NPR = 4.2. The Reynolds stress anisotropy shows a strong dependence on nozzle pressure ratio. At NPR = 2.2 there are peaks of anisotropy in the jet core, located just downstream of the centreline shock and expansion wave positions. These centreline peaks are not seen at higher pressures. At NPR = 2.2 the jet instability process is dominated by the m=0 (axisymmetric) instability mode, and these centreline peaks in anisotropy may be due to the interaction between toroidal vortex structures and the jet shocks. Towards the end of the potential core the magnitude of the $\overline{v'v'}$ stresses begin to exceed the $\overline{u'u'}$ stresses. After the shear layer merges at the jet centreline, the flow moves closer to isotropy, though the axial stresses remain slightly stronger than the transverse stresses.

As pressure ratio increases, the topology of the anisotropy within the jet changes. The strong peaks in anisotropy on the centreline disappear, and the degree by which the transverse stresses exceed the axial stresses near the end of the potential core increases significantly. This region of stronger transverse stress also appears to extend over a greater axial domain with increasing pressure (though this pattern does not hold once the Mach disk begins to grow in size). For NPR = 2.6, the jet instability process is characterized by a phase locked azimuthal modes $m = \pm1$, resulting in a flapping instability. For NPR = 3.4 & 4.2, a single helical mode is dominant.

At higher pressures the peaks in Reynolds stress anisotropy move from the centreline of the flow to the shear layer, and a periodic modulation of the degree of anisotropy at the shock-reflection points is clearly evident, with the degree of modulation increasing with increasing shock strength. Prior work has shown that the periodic shock cells modulate the axial velocity fluctuations most strongly in the shear layer, and the transverse fluctuations most strongly at the centreline (Edgington-Mitchell *et al.*, 2014*b*). At NPR = 4.2 the large Mach disk is seen to produce local regions of extremely high anisotropy. This may be a combination of the PIV technique producing artificial velocity fluctuations across the Mach disk (Mitchell *et al.*, 2011) and the transverse oscillation of shock position due to the passage of coherent shear layer vortices. Further discussion in this paper will focus on the NPR = 4.2 jet, which has been previously presented in Edgington-Mitchell *et al.* (2014*a*).
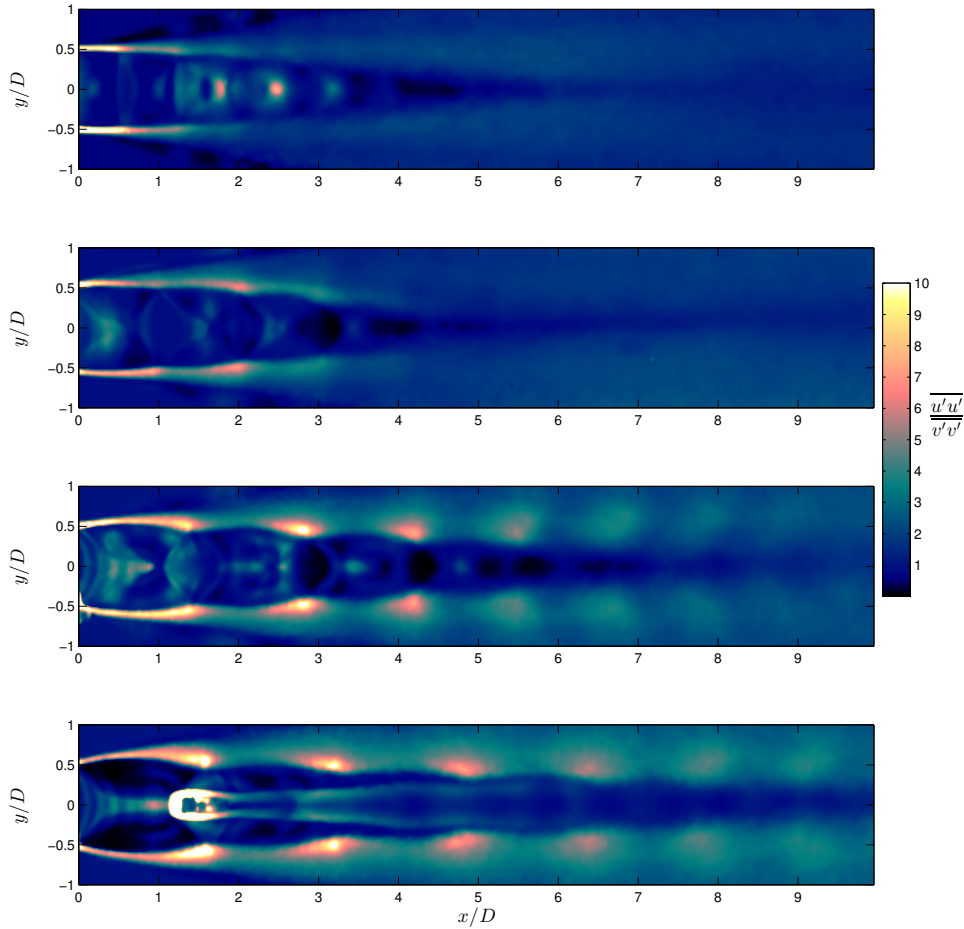
Figure 2. Experimentally determined contours of two-component Reynolds stress anisotropy for underexpanded jets at pressures (from top to bottom) NPR = 2.2, 2.6, 3.4, 4.2.

The numerical dataset offers the potential to consider the anisotropy with respect to the out-of-plane velocity component, as well as removing the effects of seed particle lag on the measurement of fluctuating velocity in the near-shock regions. The experimental and numerical datasets are not intended for direct comparison; the validation role of the experimental data here is qualitative rather than quantitative. Figure 3 presents a comparison of the numerically and experimentally determined axial Reynolds stress for the jet at NPR = 4.2. The overall structure of the flow is very similar in both cases, with the key features identified in the experimental data replicated in the simulations. The modulation of the axial Reynolds stresses at the shock reflection points within the shear layer is well captured by the simulation. The axial Reynolds stresses in the shear layer are significantly higher for the simulation in the first two shock cells, but the discrepancy reduces further downstream. This may be due to the much thinner initial shear layer in the numerical simulation.

A comparison of the anisotropy of the $\overline{u'u'}$ and $\overline{v'v'}$ stresses is presented in Figure 4. Both numerical and experimental datasets predict a high degree of turbulent anisotropy in the shear layer near the nozzle, though the anisotropy is stronger in the experiment. Direct comparisons of the initial shear layer are difficult, due to the different inlet conditions. Both experimental and numerical data show that the degree

of anisotropy is modulated at the shock reflection points, through the modulation of the axial component demonstrated above. The modulation of anisotropy appears much stronger in the experimental data than in the numerical data however. In both datasets the highest degree of anisotropy is located in the inner shear layer generated downstream of the Mach disk triple-point. The largest discrepancy between the experimental and numerical datasets is in the region preceding the first set of oblique shock waves. In the experimental dataset, the transverse shear stress is stronger than the axial stress by a factor of five in this region. In the numerical results however, the axial stresses dominate the transverse stresses.

Having established that the numerical simulation appears to capture the key features revealed in the experimental data, it can be used to explore quantities not accessible in the experiment, such as the complete Reynolds stress tensor. Contours of four of the remaining terms from the Reynolds stress tensor are presented in Figure 5. $\overline{u'u'}$ was presented in Figure 3, and $\overline{v'w'}$ is small enough to be negligible. The radial ($\overline{v'v'}$) and azimuthal ($\overline{w'w'}$) stresses are concentrated primarily in the outer shear layer, and are both weaker than the axial stresses. These is also no evidence of modulation at the shock reflection points. The normal stress ($\overline{u'v'}$) is primarily concentrated on the inner shear layer downstream of the Mach disk triple-point, while $\overline{u'w'}$ is generally of much
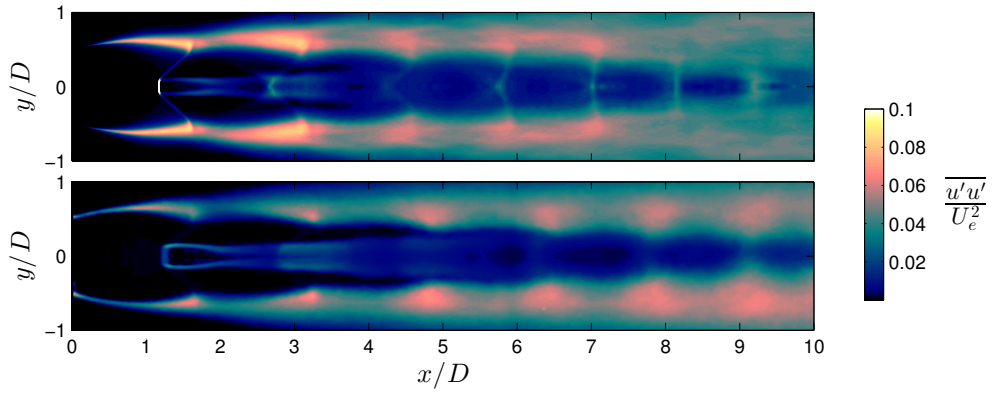
Figure 3. Comparison of numerical (top) and experimental (bottom) axial Reynolds stress $\overline{u'u'}$ for NPR = 4.2.
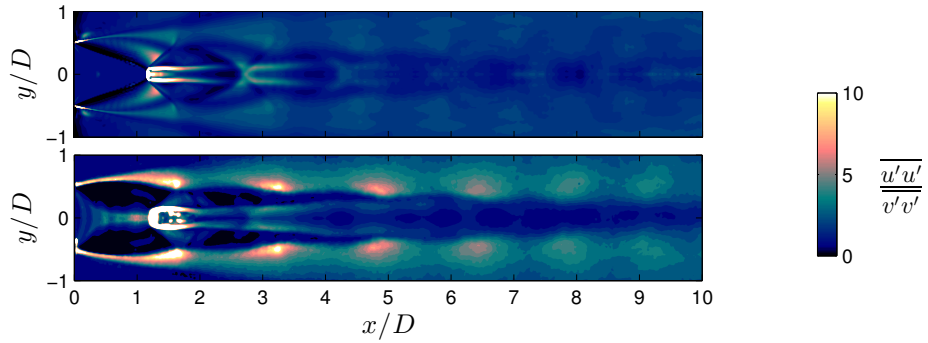
Figure 4. Comparison of numerical (top) and experimental (bottom) two-component Reynolds stress anisotropy for NPR = 4.2

lower magnitude, and focused in the outer shear layer. As mentioned, $\overline{v'w'}$ is very small relative to the other stresses.

The spatial development of the anisotropy of the turbulence can be quantified by the traceless Reynolds-stress anisotropy tensor:

$$b_{ij} = \frac{\overline{u_i'u_j'}}{2k} - \frac{1}{3}\delta_{ij} \, , \qquad (1)$$

where $k = \overline{u_l'u_l'}/2$ is the turbulent kinetic energy, and δ_{ij} is the Kronecker delta.

The two non-zero invariants of this tensor are $I_2 = -b_{ij}b_{ji}/2$ and $I_3 = b_{ij}b_{jk}b_{ki}/3$. The bounds of physically realisable solutions in this invariant space form the Lumley triangle (Lumley, 1978). These bounds identify the limiting conditions of isotropic turbulence, anisotropic turbulence with two dominant fluctuating components, and anisotropic turbulence with one dominant component. In this invariant space, we illustrate how the anisotropy along profiles normal to the jet axis evolves in the streamwise direction.

Here we present the results in the scaled invariant coordinates of $\eta = (-I_2/3)^{1/2}$ and $\zeta = (I_3/2)^{1/3}$. For further details refer to section 11.3.2 of Pope (2000).

Figure 6 presents a pair of radial profiles in invariant space. In the region preceding the Mach disk at $x/D = 0.5$, the trajectory is relatively simple, with the one-component

turbulence on the centreline rapidly giving way to primarily two component turbulence through the jet shear layer. Referring to Figures 3 and 5, this is representative of the $\overline{u'u'}$ and $\overline{w'w'}$ being of similar magnitude in the initial shear layer, while $\overline{v'v'}$ is somewhat weaker. At $x/D = 1.92$ the flow is far more complex, with the radial profile traversing through the annular internal shear layer, shock and expansion waves, then the jet outer shear layer. This renders Figure 6 very difficult to interpret, as the turbulence rapidly switches between axisymmetric and completely anisotropic along the radial profile, before finally approaching a two-component limit outside the shear layer.

To better elucidate the complex anisotropy in the flow, an alternative method of presenting the relationship between the invariants is presented. Figure 7 presents a colourmap based on the relationship between the invariants of the anisotropy tensor. A deep red is used to indicate isotropic turbulence, green indicates single component axisymmetric, while blue indicates two-component axisymmetric turbulence. Figure 8 presents the spatial variation of anisotropy in the jet at NPR = 4.2, based on the colourmap defined in Figure 7. The incredible complexity produced by the shock structures within the jet is immediately apparent. A full description of the field is beyond the scope of this work, and the discussion will be constrained to the region prior to the second shock cell. Even the initial region near the nozzle exit reveals a relatively complex structure, generally dominated by single component turbulence, but

4
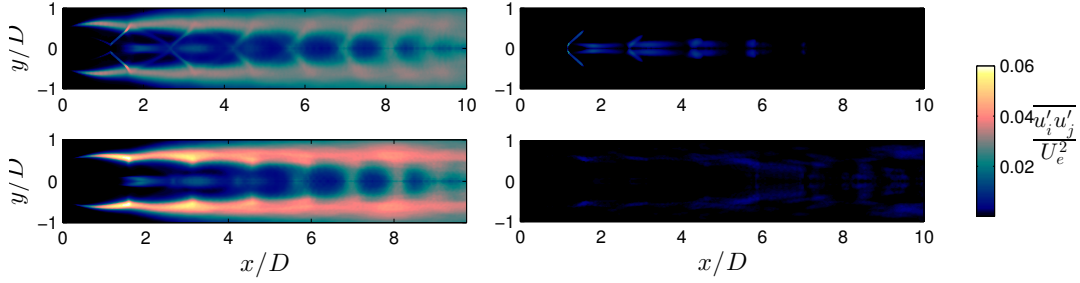
Figure 5. Reynolds stresses for NPR = 4.2 (numerical). Top Left) $\overline{v'v'}$, Top Right) $\overline{u'v'}$, Bottom Left) $\overline{w'w'}$, Bottom Right) $\overline{u'w'}$
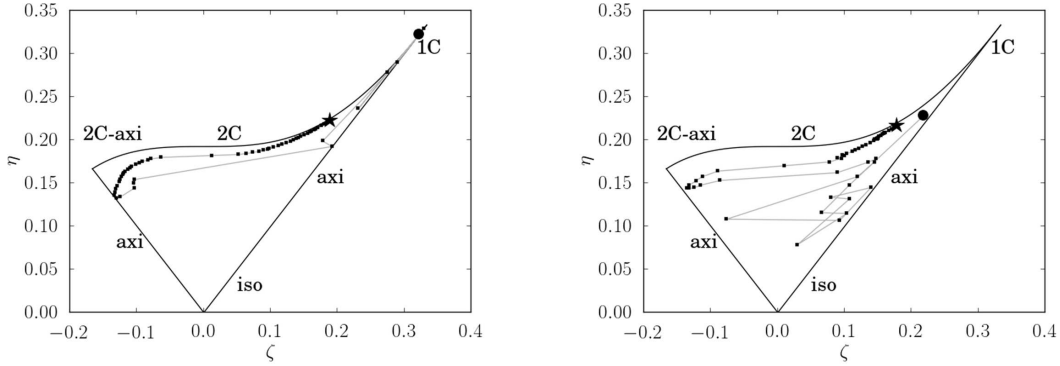
Figure 6. Reynolds stress profiles perpendicular to the centreline of the NPR = 4.2 jet, illustrated in Lumley triangle invariant space. Circular symbol is at the jet centreline $y/D = 0.01$, the star symbol is well outside the jet shear layer $y/D = 5$. Left) $x/D = 0.5$, Right) $x/D = 1.92$

with pockets of three component turbulence as well. The oblique shocks that coalesce from the reflected compression waves change the structure of the turbulence. At the shocks themselves, the fluctuations are dominated by a single Reynolds stress term, the $\overline{v'v'}$. This may be more to do with oscillations in the position of the shock, rather than any fundamental change in the nature of the turbulence. Past the shocks, the turbulence assumes a more axisymmetric character, though still largely dominated by a single component. The Mach disk is once again characterized by almost purely one component turbulence, though here it is the $\overline{u'u'}$ term that dominates. This is once again likely due to the oscillatory motion of the shock, and is consistent with DNS results of canonical shock/turbulence interaction (Larsson & Lele, 2009). Downstream of the Mach disk, it would be expected from prior studies that the turbulence be primarily axisymmetric, with the axial stresses significantly larger than the other two components. However the generation of shear from the triple point rapidly obscures any such effect, with the flow downstream of the disk dominated by the inner shear layer. This shear layer is characterized by one component turbulence ($\overline{u'u'}$) on the high speed side, and axisymmetric turbulence on the low speed side, with $\overline{u'u'}$ still the dominant component. The core of the internal post-shock region rapidly evolves however, and by $x/D \approx 2$, the flow at the centreline has instead become two component axisymmetric, with $\overline{v'v'}$ and $\overline{w'w'}$ both significantly larger than $\overline{u'u'}$.

At the outer edge of the jet, the shear layer is characterized by a region of three component turbulence, bound on the high speed side by axisymmetric turbulence with a single dominant component, and on the low speed side by two-component axisymmetric turbulence. Of particular note is the influence on the anisotropy within the shear layer of the oblique shocks extending from the triple point. At the tip of the oblique shocks, just prior to the reflection point, the flow transitions from completely three-component to something more closely approximating two-component axisymmetric. This is indicative of the shock's influence on $\overline{u'u'}$ and $\overline{v'v'}$, but no apparent influence on $\overline{w'w'}$. The relatively strong modulation of the $\overline{u'u'}$ component by the shocks is in contrast to the experimental dataset, where only a modulation of $\overline{u'u'}$ was evident. That modulation was indicated to primarily be constrained to the coherent large scale structures, rather than the stochastic fluctuations.

Conclusions

The anisotropy of the Reynolds stress tensor in shock-containing jets has been examined. The highly anisotropic nature of the Reynolds stresses in these shock containing flows has been revealed, with the flow within the jet ranging from near isotropy to full three-component turbulence. Reasonable agreement between a numerical and experimental dataset was demonstrated, especially considering the different boundary conditions of the two cases. The numerical
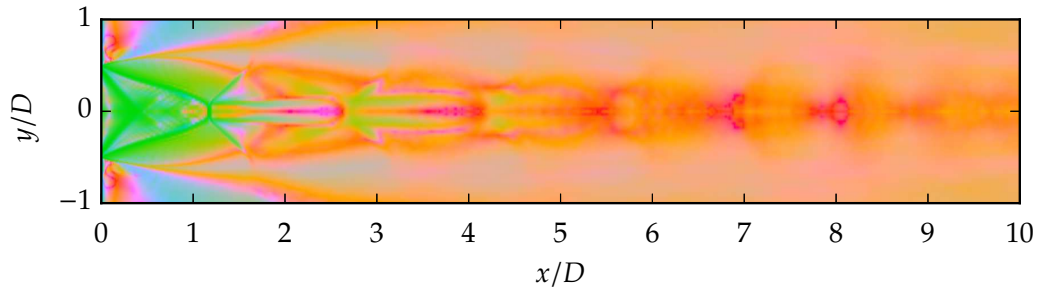
Figure 8.   Reynolds stress profile colourmap in Lumley triangle invariant space for jet at NPR = 4.2.
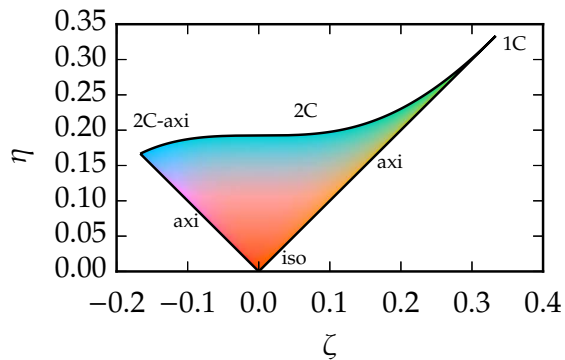
Figure 7.   Colourmap for representing the relationship between the invariants of the Reynolds-stress anisotropy tensor.

dataset (potentially due to the thicker shear layer), predicted less modulation of the anisotropy within the shear layer than was evident in the experimental data, but still captured the phenomenon clearly.

Acknowledgements

REFERENCES

Bodony, D. & Lele, S. 2005 On using large-eddy simulation for the prediction of noise from cold and heated turbulent jets. *Phys. Fluids* **17**, 85–103.

Bradshaw, Peter, Ferriss, David H & Johnson, RF 1964 Turbulence in the noise-producing region of a circular jet. *Journal of Fluid Mechanics* **19** (04), 591–624.

Edgington-Mitchell, Daniel, Honnery, Damon R & Soria, Julio 2014*a* The underexpanded jet mach disk and its associated shear layer. *Physics of Fluids (1994-present)* **26** (9), 096101.

Edgington-Mitchell, Daniel, Oberleithner, Kilian, Honnery, Damon R & Soria, Julio 2014*b* Coherent structure and sound production in the helical mode of a screeching axisymmetric jet. *Journal of Fluid Mechanics* **748**, 822–847.

Goldstein, M & Rosenbaum, B 1973 Effect of anisotropic turbulence on aerodynamic noise. *The Journal of the Acoustical Society of America* **54** (3), 630–645.

Khavaran, Abbas 1999 Role of anisotropy in turbulent mixing noise. *AIAA journal* **37** (7), 832–841.

Larsson, Johan & Lele, Sanjiva K 2009 Direct numerical simulation of canonical shock/turbulence interaction. *Physics of Fluids (1994-present)* **21** (12), 126101.

Lighthill, Michael J 1952 On sound generated aerodynamically. i. general theory. *Proceedings of the Royal Society of London. Series A. Mathematical and Physical Sciences* **211** (1107), 564–587.

Lilley, GM 1948 *On the noise from air jets*. Aeronautical Research Council, Noise Research Committee.

Lilly, D. 1992 A proposed modification of the germano subgrid-scale closure method. *Physics of Fluids* **4**, 633.

Lumley, J. L. 1978 Computational modelling of turbulent flows. *Adv. Appl. Mech.* **18**, 123–176.

Mitchell, D., Honnery, D. & Soria, J. 2011 Particle relaxation and its influence on the particle image velocimetry cross-correlation function. *Exp Fluids* **51**, 933–947.

Mitchell, Daniel M, Honnery, Damon R & Soria, Julio 2013 Near-field structure of underexpanded elliptic jets. *Experiments in fluids* **54** (7), 1–13.

Poinsot, T. 1992 Boundary conditions for direct simulations of compressible viscous flows. *J. Comput. Phys.* **99**, 352.

Pope, Stephen B 2000 *Turbulent flows*. Cambridge university press.

Ribner, Herbert S 1969 Quadrupole correlations governing the pattern of jet noise. *Journal of Fluid Mechanics* **38** (01), 1–24.

Schlichting, H. & Gersten, K. 2000 *Boundary Layer Theory*. Springer.

Soria, J. 1996 An investigation of the near wake of a circular cylinder using a video-based digital cross-correlation particle image velocimetry technique. *Experimental Thermal and Fluid Science* **12**, 221–233.

Tam, C. 1995 Supersonic jet noise. *Annu. Rev. Fluid Mech.* **27**, 17–43.